RSC Advances

PAPER

View Article Online
View Journal | View Issue



Cite this: *RSC Adv.*, 2019, **9**, 10889

# Multifunctional $BiF_3$:$Ln^{3+}$ (Ln = Ho, Er, Tm)/$Yb^{3+}$ nanoparticles: an investigation on the emission color tuning, thermosensitivity, and bioimaging†

Xinxin Yan,[a] Tiesheng Li,*[a] Linna Guo,[a] Honglei Li,[a] Penglei Chen[b] and Minghua Liu[b]

Received 8th February 2019
Accepted 18th March 2019

DOI: 10.1039/c9ra01018a

rsc.li/rsc-advances

Pure cubic phase and uniform $BiF_3$:$Ln^{3+}$ (Ln = Ho, Er, Tm)/$Yb^{3+}$ nanoparticles (NPs) were prepared by coprecipitation. The growth mechanism of $BiF_3$:2%$Er^{3+}$/20%$Yb^{3+}$ NPs was proposed based on evolution analysis of the time-dependent morphology, in which $BiF_3$:2%$Er^{3+}$/20%$Yb^{3+}$ was formed through the growth process of "nucleation to crystallization and Ostwald ripening". The upconversion luminescence (UCL) properties and mechanism of $BiF_3$:$Ln^{3+}$ (Ln = Ho, Er, Tm)/$Yb^{3+}$ under dual-wavelength excitation were also systematically investigated. The emission intensity of $BiF_3$:2%$Er^{3+}$/20%$Yb^{3+}$ by dual-wavelength excitation ($\lambda$ = 980 nm + 1550 nm) was 1.49 times more than that excited by 1550 nm or 980 nm individually. Furthermore, the properties of the bright white and multicolor UCL showed that yellow, purple, green, or pinkish light could be observed by controlling the doping concentration of $Ln^{3+}$ (Ln = Yb, Er, Tm, and Ho), indicating that they had potential applications in backlight sources of color displays and security labeling. The temperature sensitivity of $BiF_3$:2%$Er^{3+}$/20%$Yb^{3+}$ exhibited a downward tendency and its max value was about 0.0036 $K^{-1}$ at 273 K. Cell toxicity tests showed that the UCNPs in phospholipid aqueous solution presented low cytotoxicity. Also, *in vivo* imaging and X-ray imaging revealed that the $BiF_3$:2%$Er^{3+}$/20%$Yb^{3+}$ NPs had deep penetration and high contrast, which meant it could be used as a potential probe and contrast agent in *in vivo* optical bioimaging.



## 1. Introduction

Recently, UCNPs doped with lanthanides (Ln) have made considerable progress.[1–7] Compared to organic dyes and conventional quantum dot materials, $Ln^{3+}$-doped UCNPs are better in terms of chemical stability, toxicity, optical stability, luminous life, and emission peak, resulting in UCNPs having the advantages of weak auto-fluorescence, low radiation damage, and deep tissue penetration.[8–16] Therefore, they have great potential in different fields.[17] It is well known that UC emission can be accurately controlled through adjusting the concentrations of different activator ions ($Er^{3+}$, $Tm^{3+}$, $Ho^{3+}$). Also, white and multicolor UCLNPs have attracted much attention due to their potential applications in backlight sources in color displays and security labeling.[18,19]

It is well known that matrix selecting is an important factor to get desired UCL, in which various host materials, such as sulfide, fluorides, oxygenated compounds, can be used for UC emissions.[20–22] Among these, fluorides are considered as excellent hosts because of their relatively lower cut-off phonon frequency and lower non-radiative relaxation.[23–27] Zhang *et al.* reported the excellent matrix $NaBiF_4$ without a rare earth ion fabricated by a super facile synthetic method, in which the reaction only took 1 min at room temperature.[28] Yu *et al.* used the same method to synthesize $NaBiF_4$:$Yb^{3+}$/$Er^{3+}$ NPs and $BiF_3$:$Yb^{3+}$/$Er^{3+}$ NPs and investigated their UCL properties and temperature sensitivity.[29,30] However, investigations on multicolor UCL, UCL excited by dual-wavelength, and the bioimaging of $BiF_3$:$Yb^{3+}$/$Er^{3+}$ have not been performed yet, but are very important for their application.[5,18,31] Herein, this motivated us to further study these excellent matrix $BiF_3$:$Yb^{3+}$/$Ln^{3+}$ (Ln = Ho, Er, Tm) NPs in a deeper investigation.

In this work, the cubic phase of $BiF_3$:$Ln^{3+}$ (Ln = Ho, Er, Tm)/$Yb^{3+}$ UCNPs was designed and synthesized by the same facile strategy. Their UCL properties were investigated by excitation at 1550 nm and 980 nm, simultaneously. The growth mechanism and the effect of time on their morphology was also explored. The function of different doped concentrations of $Er^{3+}$, $Ho^{3+}$, and $Tm^{3+}$ ions for the multicolor and white emission were also

[a]College of Chemistry and Molecular Engineering, Zhengzhou University, The Key Lab of Chemical Biology and Organic Chemistry of Henan Province, The Key Lab of Nano-information Materials of Zhengzhou, Zhengzhou, 450001, P. R. China. E-mail: lts34@zzu.edu.cn

[b]Beijing National Laboratory for Molecular Science, Institute of Chemistry, Chinese Academy of Sciences, Beijing, 100190, P. R. China

† Electronic supplementary information (ESI) available. See DOI: 10.1039/c9ra01018a

investigated. *In vivo* and X-ray imaging of the $BiF_3$:2%$Er^{3+}$/20% $Yb^{3+}$ NPs were studied.

## 2. Experimental

### 2.1 Preparation

All reagents were purchased from Aladdin Chemical Reagent Factory (China) in this research and used without further treatment. The synthesis of the cubic $BiF_3$:$Ln^{3+}$/$Yb^{3+}$ UCNPs proceeded as reported in ref. 30 (see ESI†).

### 2.2 Characterization

Details on the instruments used are presented in the ESI.†

### 2.3 *In vitro* cytotoxicity evaluation, and *in vivo* and X-ray imaging

The relevant evaluation[32] of cytotoxicity *in vitro* and *in vivo* and X-ray imaging were presented in ESI.†

## 3. Results and discussion

### 3.1 Characterization of the phase and morphology

The crystal phases of $BiF_3$:$Ln^{3+}$/$Yb^{3+}$ NPs were determined by XRD as shown in Fig. 1, in which they presented similar crystal cubic phases (JCPDS: 51-0944). The SEM image of $BiF_3$:2%$Er^{3+}$/20%$Yb^{3+}$ NPs, as an example, exhibited regular NPs (Fig. 2a), which was confirmed by the TEM image (Fig. 2b). Fig. 2c shows that the *d*-spacing was 0.13 nm, which matched with the crystal plane (331) of the cubic phase $BiF_3$ NPs. According to the results of element mapping (Fig. 2d–g), it was clear that the elements of Bi, Yb, Er, and F were uniform on the NPs. These elements were also confirmed by the EDX spectrum (Fig. 2h). $BiF_3$:20% $Yb^{3+}$,0.5%$Tm^{3+}$/2% $Ho^{3+}$ are presented in Fig. S1† and their SEM images are shown in Fig. S2,† which further illustrates the formation of $BiF_3$:$Ln^{3+}$(Ln = Ho, Er, Tm)/$Yb^{3+}$ UCNPs.

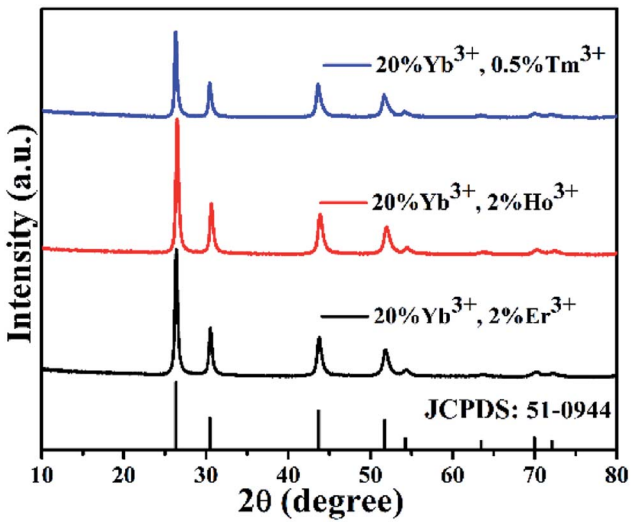


Fig. 1 XRD patterns of $BiF_3$:$Ln^{3+}$/$Yb^{3+}$.

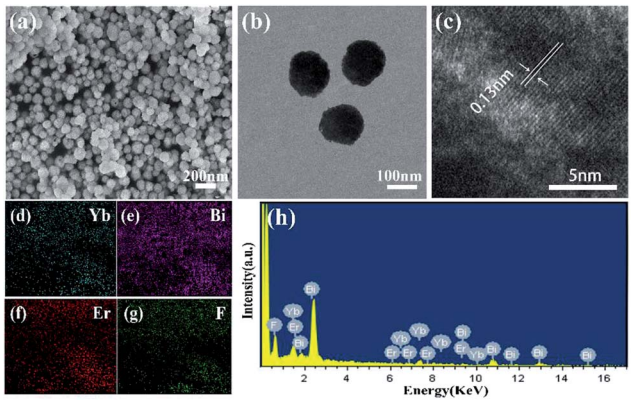


Fig. 2 Characterization of $BiF_3$:2%$Er^{3+}$/20%$Yb^{3+}$ NPs: (a) SEM image, (b) TEM image, (c) HRTEM image, (d–g) elemental mappings of Yb, Bi, Er, and F, (h) energy-dispersive X-ray (EDX) spectrum.

The XPS of $BiF_3$:2%$Er^{3+}$/20%$Yb^{3+}$ NPs was measured (Fig. S3a†). Two peaks centered at 159.9 eV and 165.1 eV were assigned to Bi $4f_{7/2}$ and Bi $4f_{5/2}$ (Fig. S3b†). The peaks located at 684.4, 165.3, and 186.1 eV were attributed to the $BiF_3$:2%$Er^{3+}$/20%$Yb^{3+}$ NPs of Yb 4d, F 1s, and Er 4d, respectively (Fig. S3c–e†).

The stability of the $BiF_3$:2%$Er^{3+}$/20%$Yb^{3+}$ NPs was investigated. The TG-DSC curve (see Fig. S4†) showed that the NPs had a mild loss of weight below 600 °C. The loss of water or crystalline water could be calculated at about 100 °C. When heated at 200 °C, the glycol on the surface of the sample gradually disappeared, and the surface defects of the sample gradually decreased. When the temperature reached up to 600 °C, the sample itself began to decompose and then the mass declined linearly.

To verify whether the reaction time affected the phase and morphology, XRD patterns and SEM/TEM images of $BiF_3$:2% $Er^{3+}$/20%$Yb^{3+}$ NPs prepared at different reaction times were investigated (Fig. 3 and 4). The results showed that the diffraction peaks matched with $BiF_3$ (JCPDS: 51-0944), indicating that the prepared compounds were single phase and had better crystallinity (Fig. 3). It can be seen from Fig. 3b that the diffraction peaks at 26.34° of $Yb^{3+}$, $Er^{3+}$-doped $BiF_3$ had a slight shift compared to $BiF_3$ (JCPDS: 51-0944). The reason should be that the ionic radii of both $Er^{3+}$ (1.004 Å) and $Yb^{3+}$ (0.985 Å) are

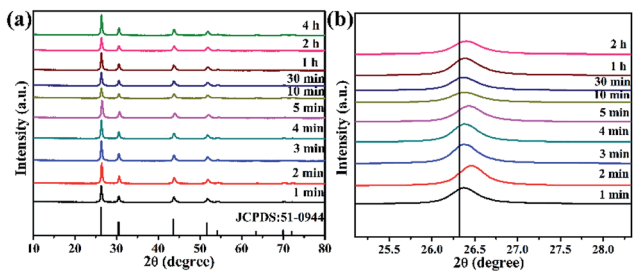


Fig. 3 (a) XRD patterns of $BiF_3$:2%$Er^{3+}$/20%$Yb^{3+}$ NPs obtained at different reaction times, (b) shifts of the main diffraction peaks of $BiF_3$:2%$Er^{3+}$/20%$Yb^{3+}$ NPs.

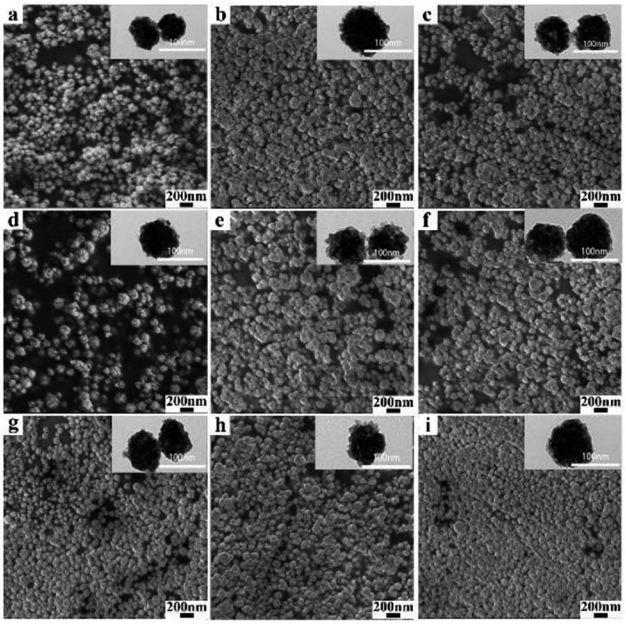


Fig. 4 SEM and TEM images of $BiF_3$:2%$Er^{3+}$/20%$Yb^{3+}$ NPs obtained at different reaction times: (a) 2 min, (b) 3 min, (c) 4 min, (d) 5 min, (e) 10 min, (f) 30 min, (g) 1 h, (h) 2 h, and (i) 4 h.

smaller than that of $Bi^{3+}$ (1.17 Å). In the $BiF_3$ host lattice, the ions ($Yb^{3+}$, $Er^{3+}$) could enter the $BiF_3$ crystal site through substituting for the $Bi^{3+}$ ions or in the interstitial sites or could coexist in these two ways. Different doping methods could make the XRD peaks of the samples prepared at different time shift by different degrees. This indicated that $Yb^{3+}$ and $Er^{3+}$ had been doped into the $BiF_3$ matrix.[33] The XRD of $BiF_3$:20%$Yb^{3+}$,0.5% $Tm^{3+}$/2%$Ho^{3+}$ showed similar results, as shown in Fig. S5.†

The SEM and TEM images of $BiF_3$:2%$Er^{3+}$/20%$Yb^{3+}$ obtained at different reaction times are presented in Fig. 4. It can be clearly observed that there are a large number of well-dispersed NPs with similar morphologies, indicating that the morphologies were almost unchanged even as the time was prolonged, which was confirmed by the TEM images (insets of Fig. 4). In addition, $BiF_3$:20%$Yb^{3+}$,2%$Ho^{3+}$/0.5%$Tm^{3+}$ in Fig. S6 and S7† showed similar results.

In order to better understand the formation process of $BiF_3$:2%$Er^{3+}$/20%$Yb^{3+}$ within 1 min, the growth mechanism was carefully studied by XRD and TEM at different reaction times (5, 30, 50, and 60 s), as shown in Fig. S8† and 5. Some impurity peaks emerged compared with the standard peaks in 5 s (Fig. S8†) and some small particles appeared in the TEM (Fig. 5a), indicating that the crystal nucleus was completed quickly. As the reaction time was further increased, the impurity peaks gradually disappeared (Fig. S8†) and the basic $BiF_3$ spheroids gradually further grew or aggregated (see Fig. 5b and c). These could be deemed as indicating the ripening process of $BiF_3$ NPs, meaning that larger spherical NPs were gradually formed due to the thermodynamic minimization of the surface energies of smaller particles, which is commonly known as Ostwald ripening.[34] $BiF_3$:2%$Er^{3+}$/20%$Yb^{3+}$ with regular morphologies were formed and the whole system achieved equilibrium when the time was 1 min (Fig. 5d). Meanwhile, XRD patterns were well matched with the pure cubic phase of $BiF_3$ (Fig. S8†). Based on the morphology evolution, the possible growth mechanism is proposed as follows (Scheme 1). First, the precursor was converted to $BiF_3$:2%$Er^{3+}$/20%$Yb^{3+}$ nuclei in the nucleation stage. Subsequently, the nuclei grew to rudimental NPs and then underwent the Ostwald ripening process until well-crystallized $BiF_3$ NPs were formed, therefore the process could be described as "Nucleation → Crystallization → Ostwald ripening" (Scheme 1).

The influence of the temperature on the phase and morphology of $BiF_3$:2%$Er^{3+}$/20%$Yb^{3+}$ were also investigated by XRD, SEM, and TEM (Fig. S9† and 6). It could be seen that the XRD spectra of NPs obtained at different temperatures (−25, 0, 30, 50, and 70 °C) matched well with the standard cubic phase (Fig. S9†). No impurities peaks were found in these patterns, indicating these samples had higher purity. However, a few new diffraction peaks appeared at 100 °C, indicating that the pure cubic phase of $BiF_3$:2%$Er^{3+}$/20%$Yb^{3+}$ NPs tended to be formed at a lower temperature. Meanwhile, SEM images of $BiF_3$:2%$Er^{3+}$/20%$Yb^{3+}$ NPs synthesized at different temperatures, sizes, and morphologies also showed no obvious changes, except that they became irregular at 100 °C (Fig. S9† and 6f). The corresponding TEM images are shown in Fig. 6g–l, in which the results were in good agreement with the XRD results. From the above analysis, it could be concluded that the regular $BiF_3$:2%$Er^{3+}$/20%$Yb^{3+}$ NPs could be formed at lower temperature under co-precipitation conditions.

### 3.2 UCL of $BiF_3$:$Ln^{3+}$(Ln = Ho, Er, Tm)/$Yb^{3+}$

**3.2.1 Effect of calcination temperature on the stability of UCL.** Fig. S10† presents the UCL spectra of $BiF_3$:2%$Er^{3+}$/20% $Yb^{3+}$ excited at 980 nm for different times. It can be seen that when prepared without calcination, its emission intensity gradually increased with prolonging the irradiation time (Fig. S10a†) and reached the maximal value in 7 min. Similarly, the variation trend of the UCL intensity of $BiF_3$:2%$Er^{3+}$/20%$Yb^{3+}$

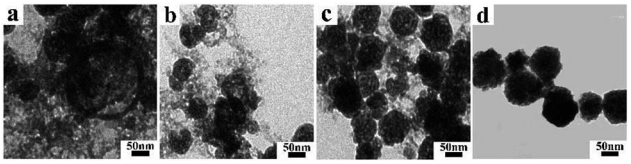


Fig. 5 TEM images of $BiF_3$:2%$Er^{3+}$/20%$Yb^{3+}$ UCNPs obtained at different reaction times: (a) 5 s, (b) 30 s, (c) 50 s, and (d) 1 min.

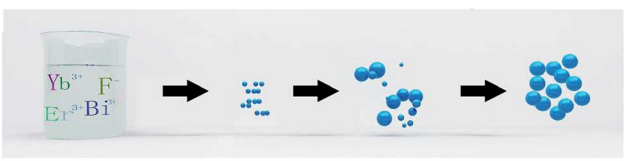


Scheme 1 Schematic of the growth mechanism of $BiF_3$:2%$Er^{3+}$/20% $Yb^{3+}$.

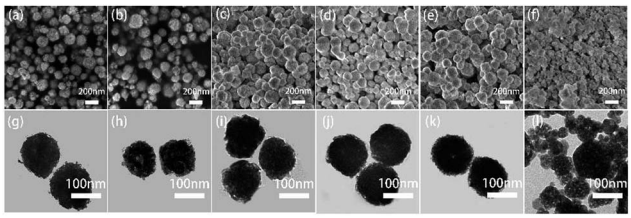


Fig. 6 SEM and TEM images of $BiF_3$:20%$Yb^{3+}$/2%$Er^{3+}$ NPs obtained at different temperatures: (a and g) −25 °C, (b and h) 0 °C, (c and i) 30 °C, (d and j) 50 °C, (e and k) 70 °C, and (f and l) 100 °C.

annealed at 50 °C was the same as that without calcination (Fig. S10b†). However, the UCL intensity did not change with increasing irradiation time when it was annealed at 100 °C, 200 °C, or 400 °C (Fig. S10c–e†). The reason for this might be that there was a large amount of hydroxyl groups (OH) on the sample's surface before calcination or certain temperature, which could increase the non-radiative relaxation rate and decrease the luminescence efficiency.[35] The results could be further confirmed by FT-IR and XRD studies of $BiF_3$:2%$Er^{3+}$/20%$Yb^{3+}$ before and after calcination. The XRD patterns and FT-IR spectra of $BiF_3$:2%$Er^{3+}$/20%$Yb^{3+}$ NPs at different calcination temperatures were recorded, as shown in Fig. S11† and 7. The diffraction peaks were matched with a cubic phase of $BiF_3$, except when annealed at 400 °C in Fig. S11.† The reason might be that the temperature reached its phase inversion temperature and then the crystalline phase began to change. The morphologies of samples calcined at different temperatures were also analyzed, as shown in Fig. S12.† From the figure, we can clearly see that the morphology of calcined samples became irregular when the calcination temperature was 400 °C. This result was consistent with the XRD results. According to the FT-IR spectra measured for the calcinated NPs (Fig. 7), the intensity of the characteristic peaks changed. The band at 552 $cm^{-1}$ arose from the vibration mode of Bi–F, which showed almost no change, but then changed at 400 °C to form another phase. The band approximately at 3388 $cm^{-1}$ and 1650 $cm^{-1}$ ascribed to O–H and some organic molecular decreased with the rising calcination temperature. The enhancement of UCL intensity might be caused by the reduction in the number of OH groups[35] and in the organic component. This was in agreement with the result of TG-DSC. $BiF_3$:2%$Er^{3+}$/20%$Yb^{3+}$ treated at 200 °C was used for the following investigation on UCL.

**3.2.2 Investigation on UCL mechanism.** The UC emission spectra of $BiF_3$:$Ln^{3+}$ (Ln = Tm, Er, Ho)/$Yb^{3+}$ NPs irradiated at 980 nm were measured and the corresponding results are given in Fig. 8a. It could be seen that there were three different colors. To better understand the mechanism of every UCL, the variation of UCL intensities with pump power density was measured (Fig. 8b–d). It is well known that the relationship between the pump power density ($P$) and luminescence intensity ($I$) is $I = P^n$, by which information of the $n$ photons in the UCL process can be provided.[36] As presented in Fig. 8b, the slopes for the 526, 547, and 656 nm bands were 1.45, 1.57, and 1.49, respectively, showing a two-photon absorption process for the $BiF_3$:2%$Er^{3+}$/20%$Yb^{3+}$ NPs. As presented in Fig. 8c, the slopes were 1.87 and 1.61 for $Ho^{3+}$ ion, meaning a two-photon process for $BiF_3$:2% $Ho^{3+}$/20%$Yb^{3+}$ NPs. The slopes for $BiF_3$:0.5%$Tm^{3+}$/20%$Yb^{3+}$ NPs were 1.97, 2.50, and 2.60, corresponding to two-photon (red NIR) and three photon (red and blue) energy-transfer processes in Fig. 8d.

The possible UCL mechanism of $Yb^{3+}$, $Er^{3+}$, $Ho^{3+}$, and $Tm^{3+}$ ions are shown in Fig. S13.† For $BiF_3$:2%$Er^{3+}$/20%$Yb^{3+}$ NPs, the $Yb^{3+}$ ion absorbs a photon and is excited to $^2F_{5/2}$, then drops back to the ground state and transfers the energy to a nearby $Er^{3+}$ ion to populate the $^4I_{11/2}$. The $Yb^{3+}$ can then transfer the second photon to populate the $^4F_{7/2}$ and relax to $^2H_{11/2}$ or $^4S_{3/2}$ levels non-radiatively. Through non-radiative relaxation, the $^4I_{11/2}$ level can also relax to the $^4I_{13/2}$ level and after that a transferred photon from $Yb^{3+}$ ions can populate the $^4F_{9/2}$. Red

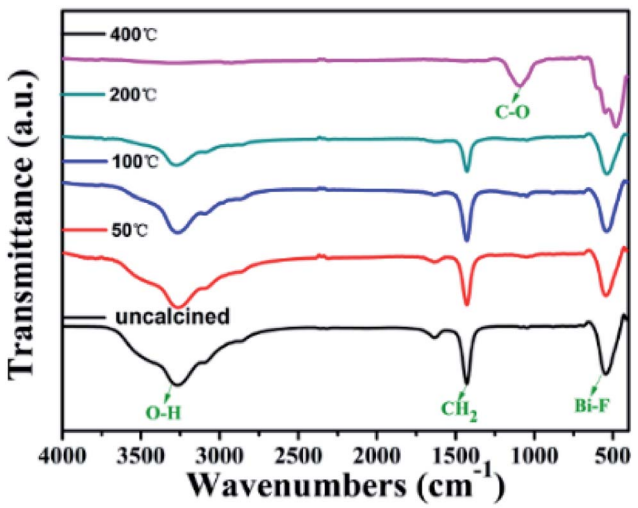


Fig. 7 FT-IR spectra of $BiF_3$:2%$Er^{3+}$/20%$Yb^{3+}$ calcinated at different temperatures.

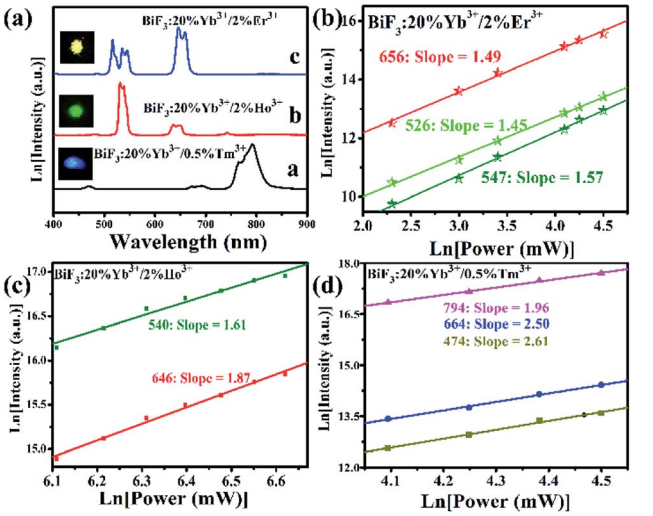


Fig. 8 (a) UC emission spectra and corresponding luminescence photographs, (b–d) pump power dependence of blue, green, red, and NIR UCL emission intensities in $BiF_3$:$Ln^{3+}$ NPs excited at 980 nm.

emission is transmitted through $^4F_{9/2} \rightarrow {}^4I_{15/2}$ of $Er^{3+}$, as shown in Fig. S13a.† The red and blue emissions of $BiF_3$:20%$Yb^{3+}$/0.5% $Tm^{3+}$ NPs could be confirmed as a three-photon process, as shown in Fig. S13b.† The $^1G_4$ level could be populated by a three-step energy transfer of $Yb^{3+}$ through $^3H_4$ and $^3F_4$. From the transitions of $^1G_4 \rightarrow {}^3F_4$, $^3H_4 \rightarrow {}^3H_6$ and $^1G_4 \rightarrow {}^3H_6$, red, NIR, and blue emissions of $Tm^{3+}$ could be obtained, respectively. As for $BiF_3$:20%$Yb^{3+}$/2%$Ho^{3+}$ NPs, red emission through the bridge of the $^5I_7$ level was pumped to the $^5F_5$ level and the green emission was then a two-photon process (Fig. S13b†).[18]

**3.2.3 Multicolor tuning and bright white emission.** In order to expand those UCNPs potential applications, the bright white and multicolor UCL has been studied. To get multicolor emission, such as bright white emission, the concentrations of $Er^{3+}$, $Ho^{3+}$, and $Tm^{3+}$ ions could be properly adjusted, in which different samples were obtained (Table S1†). The bright yellow green, pinkish, bright white, and bluish white UCL emissive spectra and photographs are shown in Fig. 9, which agreed well with the results of the color coordinate in Fig. S14.† Those results indicated that $BiF_3$ nanomaterials have potential applications as backlight sources in color displays and security labeling.

**3.2.4 Performance of UCL under dual-wavelength excitation (1550 nm and 980 nm).** It was necessary to investigate the UC process with dual-wavelength excitation, which is considered as potentially a convenient way to improve the efficiency of power conversion in next-generation solar cells.[37–39] According to Fig. 10, the ratio of green/red emission intensities was similar. Under dual-excitation at 1550 nm and 980 nm, the intensity of UCL was greater than the sum of the intensities at 1550 nm and 980 nm, respectively. It was 1.49 times the sum of the separate single wavelength excitations, indicating there was a dual-wavelength synergistic effect in this system.[40,41]

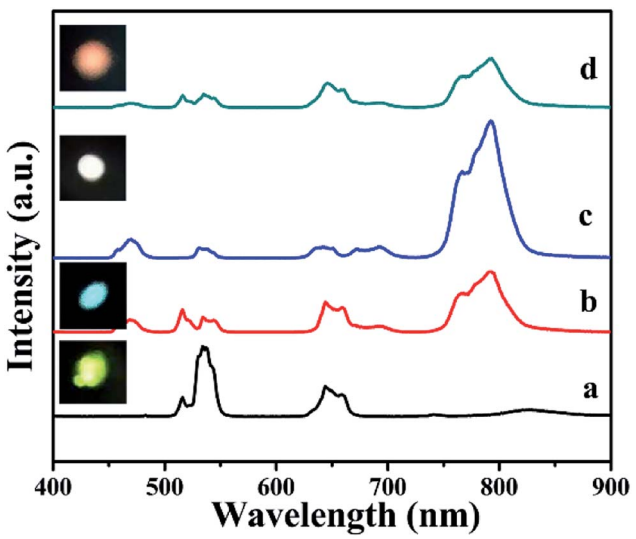


Fig. 9 UCL emissive spectra and corresponding luminescence photographs of: (a) $BiF_3$:20%$Yb^{3+}$/1%$Er^{3+}$/0.15%$Ho^{3+}$, (b) $BiF_3$:20% $Yb^{3+}$/1%$Er^{3+}$/0.5%$Tm^{3+}$, (c) $BiF_3$:20%$Yb^{3+}$/0.5%$Tm^{3+}$/0.15%$Ho^{3+}$, (d) $BiF_3$:20%$Yb^{3+}$/1%$Er^{3+}$/0.5%$Tm^{3+}$/0.15%$Ho^{3+}$ NPs excited at 980 nm.

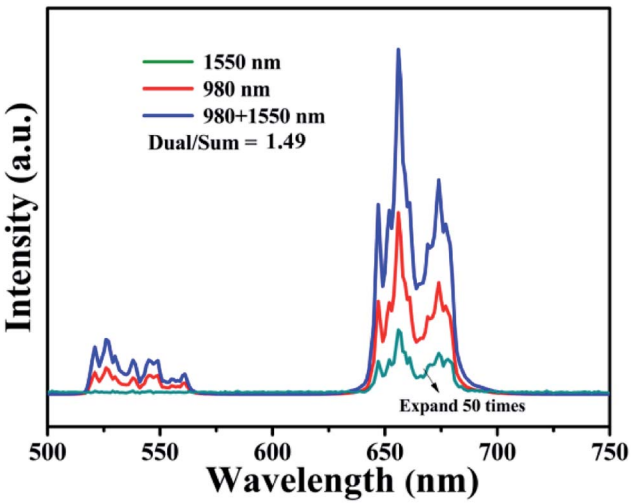


Fig. 10 UC emission spectra of $BiF_3$:2%$Er^{3+}$/20%$Yb^{3+}$ under 980 nm, 1550 nm, or simultaneous dual-wavelength (1550 nm and 980 nm) excitation ($P_{1550} = P_{980} = 100$ mW).

**3.2.5 Thermometric property of $BiF_3$:2%$Er^{3+}$/20%$Yb^{3+}$ NPs.** It was well known that the change of the transitions of $^2H_{11/2} \rightarrow {}^4I_{15/2}$ (524 nm) and $^4S_{3/2} \rightarrow {}^4I_{15/2}$ (542 nm) at different temperatures owing to $^2H_{11/2}$ and $^4S_{3/2}$ levels were related to the thermal coupling of $Er^{3+}$ ion. The ratio ($R$) of emission intensities at 524 nm and 542 nm followed the formula based on the Boltzmann distribution theory:[42–44]

$$R = I_{542}/I_{524} = A \exp - \frac{\Delta E}{kT} \quad (1)$$

where $A$ is the proportionality constant, $\Delta E$ is the energy gap between $^2H_{11/2}$ and $^4S_{3/2}$ levels, $T$ is the absolute temperature, and $k$ is the Boltzmann's constant. Eqn (1) could also be expressed as:

$$\ln(R) = -\frac{\Delta E}{kT} + \ln(A) \quad (2)$$

Fig. 11a presents the UC emission spectra of $BiF_3$:2%$Er^{3+}$/ 20%$Yb^{3+}$ excited at 980 nm with various temperatures. For green (524 nm and 542 nm) emissions, the UC emission intensities changed with increasing temperature. Fig. 11b presents a plot of $1/T$ *versus* $\ln(R)$, in which the slope ($-\Delta E/k$) is equal to $-501$ and the intercept is 1.17. It could be also seen from Fig. 11c that $R$ increased with the increasing temperature and presented a certain rule. In addition, the sensor sensitivity is another very important factor. The sensor sensitivity ($S$) can be calculated by using the following formula:[45–48]

$$S = \mathrm{d}R/\mathrm{d}T = R\left\{\frac{\Delta E}{kT^2}\right\} = A\left\{\frac{\Delta E}{kT^2}\right\}\exp\left\{-\frac{\Delta E}{kT}\right\} \quad (3)$$

It was noteworthy that the sensitivity exhibited a downward tendency with the increasing temperature from 273 K to 453 K and its max value was about 0.0036 $K^{-1}$ at 273 K (Fig. 11d), suggesting that the $BiF_3$:2%$Er^{3+}$/20%$Yb^{3+}$ NPs had a certain

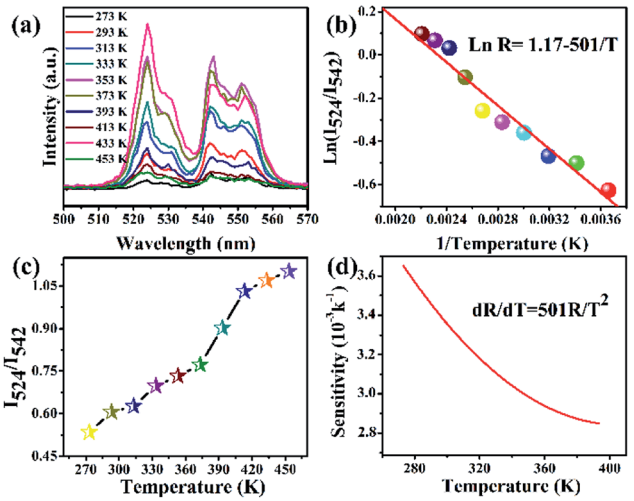


Fig. 11 (a) Green UC emission spectra of $BiF_3$:2%$Er^{3+}$/20%$Yb^{3+}$ UCNPs in the temperature range of 273–453 K, (b) plot of ln(*R*) *versus* 1/*T*. (c) *R* values of green emissions intensities at different temperatures, (d) relative sensitivity.

thermometric property, which might be employed as a temperature sensor.

**3.2.6 Cell toxicity test.** In order to evaluate the potential biosafety, cytotoxicity tests must be investigated.[49,50] As illustrated in Fig. 12, the cytotoxicity of a NPs phospholipid aqueous solution with different concentrations was assessed by CCK-8 assay under 5% $CO_2$ at 37 °C for 24 h. The viability of the B16-F10 cells decreased to 90% at a density of 1 μg $mL^{-1}$. When the concentration varied from 50 μg $mL^{-1}$ to 100 μg $mL^{-1}$, the cellular viability of B16-F10 cells decreased to 82%, indicating that the UCNPs phospholipid aqueous solution presented lower cytotoxicity.

**3.2.7 *In vivo* imaging.** 100 μL $BiF_3$:2%$Er^{3+}$/20%$Yb^{3+}$ UCNPs phospholipid aqueous solution (100 μg $mL^{-1}$) was injected into a Kunming mouse subcutaneously or intraperitoneally for deeper tissue imaging. In a comparative experiment, the luminous point on a Kunming mouse without treatment with NPs by exciting at 980 nm could not be observed with UCL (Fig. 13a and b). On the other hand, after intraperitoneal and subcutaneous injection in the corresponding area (100 μL, 100 μg $mL^{-1}$), yellow UCL could be observed in dark upon the excitation at 980 nm laser (Fig. 13c and d). These indicated that UCNPs had a high contrast and deep penetration for *in vivo* optical bioimaging, which could be used as probe.[5]

**3.2.8 *In vivo* X-ray imaging.** A certain amount of $BiF_3$:2% $Er^{3+}$/20%$Yb^{3+}$ (200 μL, 100 μg $mL^{-1}$) UCNPs phospholipid aqueous solution was injected subcutaneously in a Kunming mouse for X-ray imaging. Obvious X-ray signals marked by a white arrow could be observed for the Kunming mouse injected with NPs (Fig. 14b) compared to non-injection (Fig. 14a). It has been proven that they can absorb X-rays. The results showed that they could be utilized as X-ray imaging contrast agents.

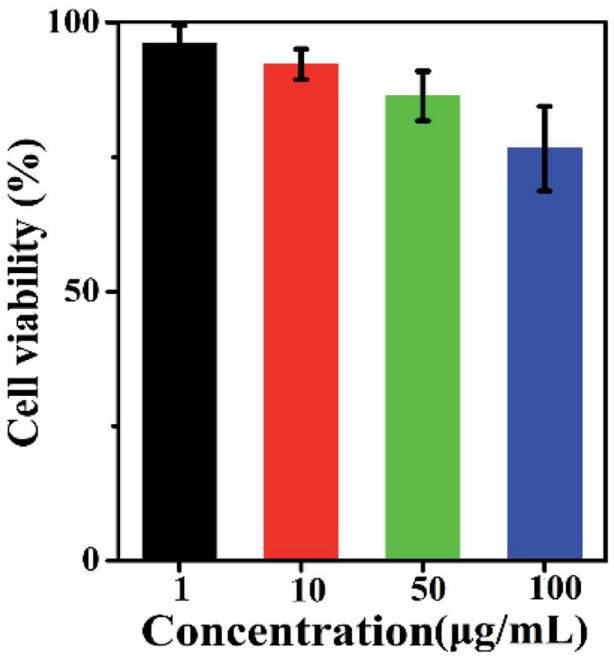


Fig. 12 Cell viability of B16-F10 cells incubated with different concentrations of $BiF_3$:2%$Er^{3+}$/20%$Yb^{3+}$ phospholipid aqueous solution.

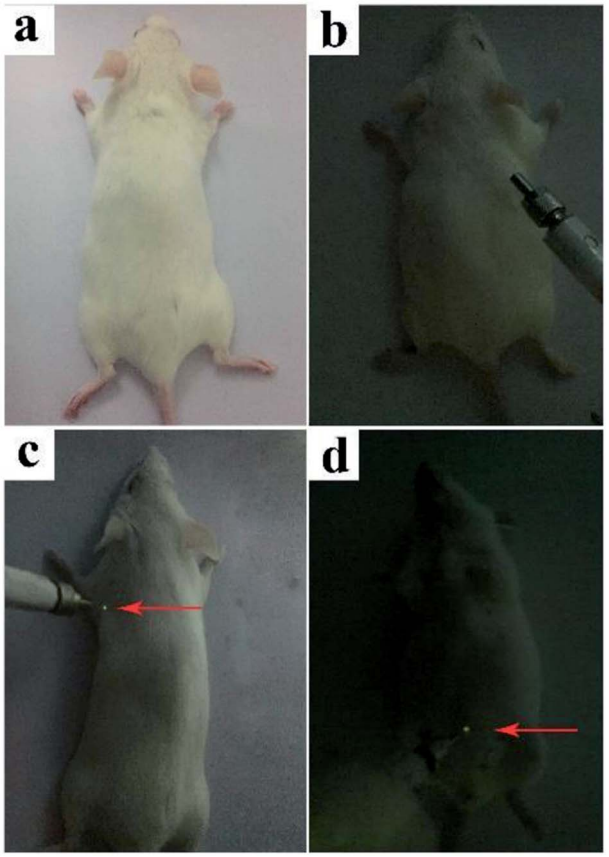


Fig. 13 *In vivo* UC imaging of a Kunming mouse: (a and b) without injection of UCNPs, (c) subcutaneous injection, and (d) intraperitoneal injection of UCNPs [100 μL (100 μg $mL^{-1}$) for c and d].

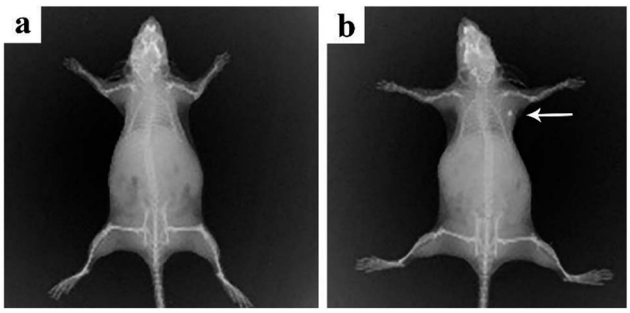


Fig. 14 *In vivo* X-ray imaging of a Kunming mouse before (a) and after (b) subcutaneous injection of 200 μL of $BiF_3$:2%$Er^{3+}$/20%$Yb^{3+}$ NPs.

## 4. Conclusions

In summary, multi-functional $BiF_3$ UCNPs were successfully synthesized by a facile co-precipitation method, both below and above room temperature (−25 °C, 100 °C). The growth mechanism indicated that the obtained $BiF_3$ NPs were formed through the growth process of "Nucleation → Crystallization → Ostwald ripening". Fluorescence intensity ratio technology was used to investigate the temperature sensitivity of $BiF_3$:2%$Er^{3+}$/20%$Yb^{3+}$ and the max sensitivity was found to be 0.0036 $K^{-1}$ at 273 K. The integrated emission of $BiF_3$:2%$Er^{3+}$/20%$Yb^{3+}$ NPs excited by dual-wavelength simultaneously was 1.49 times more than that excited by two single wavelengths (1550 nm and 980 nm), respectively. Multicolor and bright white light could be obtained upon excitation at 980 nm by modulating the content of $Ho^{3+}$, $Er^{3+}$, and $Tm^{3+}$, by which they might be used as security labeling and backlight sources for color displays. The low cytotoxicity of $BiF_3$:2%$Er^{3+}$/20%$Yb^{3+}$ was confirmed by cell toxicity tests with phospholipid aqueous solution. $BiF_3$:2%$Er^{3+}$/20%$Yb^{3+}$ NPs presented better properties of penetration and contrast in the *in vivo* imaging and X-ray imaging tests, indicating that they could be used as potential probe and contrast agents in *in vivo* optical bioimaging.

## Live subject statement

All animal procedures were performed in accordance with the Guidelines for Care and Use of Laboratory Animals of Zhengzhou University and experiments were approved by the Animal Ethics Committee of Henan Laboratory Animal Center.

## Conflicts of interest

There are no conflicts to declare.

## Acknowledgements

The authors gratefully acknowledge Chinese Academy of Sciences (Grants XDA09030203), the NSFH (142300410223) for their financial support.

## References

1 Z. W. Wei, L. N. Sun, J. L. Liu, J. Z. Zhang, H. R. Yang, Y. Yang and L. Y. Shi, *Biomaterials*, 2014, **35**, 387–392.
2 L. Y. Zeng, Y. W. Pan, R. F. Zou, J. C. Zhang, Y. Tian, Z. G. Teng, S. J. Wang, W. Z. Ren, X. S. Xiao, J. C. Zhang, L. L. Zhang, A. G. Li, G. M. Lu and A. G. Wu, *Biomaterials*, 2016, **103**, 116–127.
3 Z. M. Deng, X. L. Li, Z. L. Xue, M. Y. Jiang, Y. B. Li, S. J. Zeng and H. R. Liu, *Nanoscale*, 2018, **10**, 9393–9400.
4 Z. L. Xue, Z. G. Yi, X. L. Li, Y. B. Li, M. Y. Jiang, H. R. Liu and S. J. Zeng, *Biomaterials*, 2017, **115**, 90–103.
5 S. J. Zeng, Z. G. Yi, W. Lu, C. Qian, H. B. Wang, L. Rao, T. M. Zeng, H. R. Liu, H. J. Liu, B. Fei and J. H. Hao, *Adv. Funct. Mater.*, 2014, **24**, 4051–4059.
6 X. L. Li, Z. G. Yi, Z. L. Xue, S. J. Zeng and H. R. Liu, *Mater. Sci. Eng., C*, 2017, **75**, 510–516.
7 J. Zhou, Z. G. Lu, G. G. Shan, S. H. Wang and Y. Liao, *Biomaterials*, 2014, **35**, 368–377.
8 F. Wang and X. G. Liu, *J. Am. Chem. Soc.*, 2008, **130**, 5642–5643.
9 P. Huang, W. Zheng, S. Y. Zhou, D. T. Tu, Z. Chen, H. M. Zhu, R. F. Li, E. Ma, M. D. Huang and X. Y. Chen, *Angew. Chem., Int. Ed.*, 2014, **53**, 1252–1257.
10 M. Nyk, R. Kumar, T. Y. Ohulchanskyy, E. J. Bergey and P. N. Prasad, *Nano Lett.*, 2008, **8**, 3834–3838.
11 H. H. Gorris and O. S. Wolfbeis, *Angew. Chem., Int. Ed.*, 2013, **52**, 3584–3600.
12 J. Zhou, Q. Liu, W. Feng, Y. Sun and F. Y. Li, *Chem. Rev.*, 2014, **115**, 395–465.
13 G. F. Wang, Q. Peng and Y. D. Li, *J. Am. Chem. Soc.*, 2009, **131**, 14200–14201.
14 P. P. Lei, R. An, X. S. Zhai, S. Yao, L. L. Dong, X. Xu, K. M. Du, M. L. Zhang, J. Feng and H. J. Zhang, *J. Mater. Chem. C*, 2012, **18**, 1580.
15 G. Tian, Z. J. Gu, L. J. Zhou, W. Y. Yin, X. X. Liu, L. Yan, S. Jin, W. L. Ren, G. M. Xing, S. J. Li and Y. L. Zhao, *Adv. Mater.*, 2012, **24**, 1226–1231.
16 Z. X. Zhang, R. F. Cao, L. N. Guo, P. Li, C. X. Liang and T. S. Li, *New J. Chem.*, 2018, **42**, 15215–15220.
17 E. M. Chan, *Chem. Soc. Rev.*, 2015, **44**, 1653–1679.
18 Z. Wang, J. Feng, M. Pang, S. h. Pan and H. J. Zhang, *Dalton Trans.*, 2013, **42**, 12101–12108.
19 N. S. Singh, N. K. Sahu and D. Bahadur, *J. Mater. Chem. C*, 2014, **2**, 548–555.
20 X. Lu, M. Yang, L. Y. Yang, Q. L. Ma, X. T. Dong and J. Tian, *J. Mater. Sci.: Mater. Med.*, 2015, **26**, 4078–4084.
21 Z. Yin, H. Li, W. Xu, S. B. Cui, D. L. Zhou, X. Chen, Y. S. Zhu, G. S. Qin and H. W. Song, *Adv. Mater.*, 2016, **28**, 2518–2525.
22 P. P. Lei, P. Zhang, Q. H. Yuan, Z. Wang, L. L. Dong, S. Y. Song, X. Xu, X. L. Liu, J. Feng and H. J. Zhang, *ACS Appl. Mater. Interfaces*, 2015, **7**, 26346–26354.
23 H. X. Mai, Y. W. Zhang, R. Si, Z. G. Yan, L. D. Sun, L. P. You and C. H. Yan, *J. Am. Chem. Soc.*, 2006, **128**, 6426–6436.
24 X. Teng, Y. H. Zhu, W. Wei, S. C. Wang, J. F. Huang, R. Naccache, W. B. Hu, A. L. Y. Tok, Y. Han, Q. C. Zhang,

Q. L. Fan, W. Huang, J. A. Capobianco and L. Huang, *J. Am. Chem. Soc.*, 2012, **134**, 8340–8343.
25 Q. Liu, Y. Sun, T. S. Yang, W. Feng, C. G. Li and F. Y. Li, *J. Am. Chem. Soc.*, 2011, **133**, 17122–17125.
26 S. Sarkar, A. Dash and V. Mahalingam, *Chem.–Asian J.*, 2014, **9**, 447–451.
27 X. L. Wu, L. G. Xu, W. Ma, L. Q. Liu, H. Kuang, N. A. Kotov and C. L. Xu, *Adv. Mater.*, 2016, **28**, 5907–5915.
28 P. P. Lei, R. An, S. Yao, Q. S. Wang, L. L. Dong, X. Xu, K. M. Du, J. Feng and H. J. Zhang, *Adv. Mater.*, 2017, **29**, 1700505.
29 P. Du, L. H. Luo, X. Y. Huang and J. S. Yu, *J. Colloid Interface Sci.*, 2018, **514**, 172–181.
30 P. Du and J. S. Yu, *Microchim. Acta*, 2018, **185**, 237.
31 P. Li, L. N. Guo, Z. X. Zhang, T. S. Li and P. L. Chen, *Dyes Pigm.*, 2018, **154**, 242–251.
32 B. H. Wang, Y. X. Zhai, J. J. Shi, L. Y. Zhuang, W. Liu, H. J. Zhang, H. L. Zhang and Z. Z. Zhang, *J. Controlled Release*, 2017, **268**, 225–236.
33 P. Li, L. N. Guo, C. X. Liang, T. S. Li and P. L. Chen, *Mater. Sci. Eng., B*, 2018, **229**, 20–26.
34 A. M. Li, D. K. Xu, H. Lin, S. H. Yang, Y. Z. Shao and Y. L. Zhang, *Sci. Rep.*, 2016, **6**, 31366.
35 L. N. Guo, Y. H. Wang, Y. Z. Wang, J. Zhang, P. Y. Dong and W. Zeng, *Nanoscale*, 2013, **5**, 2491–2504.
36 C. X. Liang, L. N. Guo, P. Li, T. S. Li, P. L. Chen, M. H. Liu and Y. J. Wu, *J. Alloys Compd.*, 2017, **715**, 37–42.
37 P. Chen, S. L. Yu, B. B. Xu, J. C. Wang, X. W. Sang, X. F. Liu and J. R. Qiu, *Mater. Lett.*, 2014, **128**, 299–302.
38 J. J. Zhou, J. Y. Deng, H. M. Zhu, X. Y. Chen, Y. Teng, H. Jia, S. Q. Xu and J. R. Qiu, *J. Mater. Chem. C*, 2013, **1**, 8023–8027.
39 Z. Chen, G. B. Wu, H. Jia, K. Sharafudeen, W. B. Dai, X. W. Zhang, S. F. Zeng, J. M. Liu, R. F. Wei, S. C. Lv, G. P. Dong and J. R. Qiu, *J. Phys. Chem. C*, 2015, **119**, 24056–24061.
40 Z. Chen, X. W. Zhang, S. F. Zeng, Z. J. Liu, Z. J. Ma, G. P. Dong, S. F. Zhou, X. F. Liu and J. R. Qiu, *Appl. Phys. Express*, 2015, **8**, 032301.
41 Y. H. Yao, C. Xu, Y. Zheng, C. S. Yang, P. Liu, J. X. Ding, T. Q. Jia, J. R. Qiu, S. A. Zhang and Z. R. Sun, *RSC Adv.*, 2016, **6**, 3440–3445.
42 D. He, C. F. Guo, S. Jiang, N. M. Zhang, C. K. Duan, M. Yin and T. Li, *RSC Adv.*, 2015, **5**, 1385–1390.
43 C. D. S. Brites, X. J. Xie, M. L. Debasu, X. Qin, R. F. Chen, W. Huang, J. Rocha, X. G. Liu and L. D. Carlos, *Nat. Nanotechnol.*, 2016, **11**, 851.
44 G. Y. Zhang, Q. P. Qiang, S. S. Du and Y. H. Wang, *RSC Adv.*, 2018, **8**, 9512–9518.
45 W. Yu, W. Xu, H. W. Song and S. Zhang, *Dalton Trans.*, 2014, **43**, 6139–6147.
46 J. Zhang, B. W. Ji, G. B. Chen and Z. H. Hua, *Inorg. Chem.*, 2018, **57**, 5038–5047.
47 J. Zhang, X. M. Jiang and Z. H. Hua, *Ind. Eng. Chem. Res.*, 2018, **57**, 7507–7515.
48 P. Li, L. N. Guo, C. X. Liang, T. S. Li, P. L. Chen, M. H. Liu and Y. J. Wu, *RSC Adv.*, 2017, **7**, 51233–51244.
49 D. M. Yang, Y. L. Dai, J. H. Liu, Y. Zhou, Y. Y. Chen, C. X. Li, P. A. Ma and J. Lin, *Biomaterials*, 2014, **35**, 2011–2023.
50 P. Ramasamy, P. Chandra, S. W. Rhee and J. Kim, *Nanoscale*, 2013, **5**, 8711–8717.